Tunable living bacterial networks: A multi-scaled description of their self-assembly and mechanical behaviour

Samuel Charlton[1], Gavin Melaugh[2,3], Davide Marenduzzo[2], Cait MacPhee[3] and Eleonora Secchi[1]

[1]Institute of Environmental Engineering, Department of Civil, Environmental and Geomatic Engineering, ETH Zürich, Zürich, 8093, Switzerland.
[2]SUPA, School of Physics and Astronomy, University of Edinburgh, Edinburgh, EH9 3FD, UK.
[3] School of Engineering, University of Edinburgh, Edinburgh, EH9 3JL, UK.

Contributing authors: esecchi@ethz.ch;

Abstract

Bioflocculation is increasingly viewed as an alternative path towards bacterial surface colonisation and biofilm formation. This process garners less attention in the literature; however, it is important for wastewater treatment and clinical applications, and has a high potential to be exploited for producing living materials. In this work, we present an aggregating bacterial system that passively forms 3D networks. We apply the toolbox of colloidal physics to control and tune the microstructure and mechanics of the bacterial networks. We firstly augment the cell length distribution of this system by inducing filamentation via oxygen depletion. Filamentation enables the tuning of network properties, enhances aggregation, and reduces the number density required for 3D network assembly. Secondly, we tune the mechanical properties of the bacterial networks through hydrophobation, using glycoside hydrolase enzymes. This approach enables us to transition across three characteristic yielding modes, reducing and enhancing the network's mechanical strength. Our experimental findings are complemented by Langevin dynamic simulations, which provide insights into the controlling mechanism determining network assembly

and microstructure. This work establishes a paradigm towards exploiting bacterial self-assembly for the creation of living gels using biological concepts to tune the network properties, with broad applicability within wastewater treatment, industrial bioreactors and living materials.

Keywords: bacterial networks, filamentation, bioflocculation, living materials

1 Introduction

Bacteria exhibit a propensity for forming multicellular structures, whether as suspended bacterial aggregates or surface-attached biofilms [1]. The biofilm growth mode provides various advantages over planktonic growth, such as protection against physico-chemical stressors, and favors the emergence of collective behaviors such as the division of labor [2, 3]. The co-aggregation and sedimentation of bacterial aggregates are increasingly viewed as an additional pathway towards surface colonisation, over the canonical attachment of planktonic cells to a surface [4]. The process of aggregate formation and settling is known as bioflocculation. Bioflocculation is typically observed in systems of concentrated bacterial and algal suspensions such as in bioreactors and wastewater systems where cell concentrations range from 10^7 to 10^9 cells ml^{-1} [5]. Consequently, bioflocculation impacts a wide range of engineered and environmental systems and processes such as bio-remediation, bio-harvesting, gaseous exchange and pollutant sequestration [6]. The rate of biofloculation rate is physically controlled by encounter rates between cells and cell-cell cohesion strength [7]. While, in abiotic systems the colloidal particle aspect ratio and sedimentation rate are known control parameters of floc formation [8, 9], they are understudied in bioflocculation.

In biotic systems, bacteria can regulate their cellular aspect ratio in response to environmental stress, a process known as conditional filamentation [10]. This process is modulated by suppressing peptidoglycan septa formation in dividing cells and is triggered by nutrient stress, shifts in osmolarity, pH, temperature, and antibiotic exposure [11, 12]. Filamentation provides multiple geometric advantages to single cells, such as enhanced surface colonization due to increased cell contact area and increased metabolic efficiency due to a higher surface-to-volume ratio [13–16]. Despite several observations relating filamentation and floc formation, the mechanistic contribution of filamentation has yet to be systematically investigated across different length scales.

In colloidal and polymer systems, aggregation is a prerequisite towards network formation, which forms via cluster-cluster aggregation [17]. Here, the aspect ratio controls the encounter rate and crossover density between particles, whilst forces such as depletion attraction, polymer bridging and hydrophobic interactions tune particle-particle cohesion strength [18]. Combined, both of these variables directly control cluster formation and the resulting networks mechanical stability [19]. Furthermore, in model abiotic

systems, the aggregation kinetics, volume fraction and sedimentation shape individual cluster morphology and fractal structure [8, 9]. Upon formation, connected colloidal networks such as gels display collapsing dynamics, whereby the network strength is overcome by gravitational settling [20]. Although these dynamics and principles are well understood in abiotic systems, they have yet to be systematically applied to bioflocculation. Understanding the mechanisms that control bacterial network formation may then provide the building blocks, as with abiotic systems, to design living bacterial structures.

In this work, we investigate bioflocculation and network formation using a bacterial system that displays dynamics akin to colloidal gel formation. To do this, we use *Comamonas denitrificans*, a wastewater treatment bacterium with a propensity to filament. Using the dissolved oxygen concentration as a lever for controlling the length of the cells, we probe the influence of cell aspect ratio distribution and cell-cell cohesion strength on the network properties, sedimentation and mechanical behaviour of this system from macro- to microscale. Using simple Langevin dynamics simulation, we are able to map the structure and dynamics of the bacterial suspensions and networks to our experimental system, demonstrating the applicability of our colloidal approach to bacterial network design. Taken together, our findings demonstrate a path to building bacterial structures via cluster-cluster aggregation and provide two tuning mechanisms to shape their network properties and mechanical behaviour. This conceptual framework may lead to optimised bioreactor and wastewater treatment operation and inform functional living material design using bacteria.

2 Results

2.1 Oxygen depletion induces controllable filamentation

To gain a mechanistic understanding of the impact of cell aspect ratio on bioflocculation, we need a bacterium that can aggregate and form filaments. For this, we selected the organism *C. denitrificans*, a gram-negative bacterium isolated from an activated sludge plant. *C. denitrificans* is a known biofilm former that has been shown to play an important role in bioaugmentation and bioremediation [21, 22], and crucially for this work, has a propensity to filament.

C. denitrificans is known to seamlessly switch between aerobic and anoxic growth conditions [23]. Here, we exploit this trait to demonstrate that the cell length of *C. denitrificans* can be tuned by mediating the dissolved oxygen (DO) concentration in the liquid culture (Figs.1a,b). A larger headspace (45 ml) of the culture vessel gives rise to a higher dissolved oxygen concentration (5.6 mg/L, O_2+) compared to the smaller headspace (< 0.1 mg/L, O_2-) providing us with two DO concentrations (Fig.1c, see Methods) that are comparable with those found in activated sludge reactors and membrane filtration systems (0 mg/l to 4.0 mg/l) [24]. Under oxygen-limited conditions, we see the emergence of a filamentous phenotype (Fig.1b, Fig.1e) in which the cells are

on average longer (6.95μm vs 3.03 μm), and exhibit a greater polydispersity in cell length (1.27 vs 0.34)compared to the nonfilamentous phenotype. The cell length distributions for both the O_2- and O_2+ conditions are log-normally distributed, indicative of cumulative fragmented division events which occur during cellular growth (Fig.1e) [25].

We further characterise the structure of these filamentous cells using confocal light scanning microscopy (CLSM) by staining both the cellular membrane (red in Fig.1d) and cell nucleus (green in Fig.1d). The filamentous cells are characteristic of multi-nucleoid filaments, possessing a continuous cell membrane surrounding multiple individual nucleoids (red arrows highlight the filamentous morphology in Fig.1d). Finally, oxygen limitation in the O_2- condition gives rise to a slower growth rate with the doubling time increasing from 50 mins to 168 mins (Supplementary Fig. 1, Supplementary methods).

The filamentous phenotype enhances the relative number density of bacterial suspensions. In polymer systems, the number density describes the overlap frequency between polymer chains which directly influences network formation and microstructure [26]. The number density is calculated as $\mu = \frac{N}{V}$, where N is the number of cells and V is the sample volume and is used to identify the dilute, semi-dilute, and concentrated regimes [27]. To quantify the concentration regime in our system, we selected cell densities that span typical concentration ranges found in bioreactors, heavy wastewater in-fluent, and activated sludge bioreactors, namely 10^7-10^9 cells/ml [28]. For each cell concentration, the number density was calculated for the F and NF cases. To account for the log-normal cell length distributions, resulting in a volume distribution, we calculated an effective bacterial number density, μ_e, which considers the range of cell lengths (see Methods). From these distributions, we then calculated the semi-dilute concentration boundary, $\Lambda_{semi-dilute}$, and normalised μ_e by this boundary value, enabling us to compare the regime of each cell density. Both the F and NF phenotypes had a μ_e within the dilute regime (Fig.1f). However, F resulted in at least a 20-fold increase in $\frac{\mu_e}{\Lambda_{semi-dilute}}$ for comparable cell densities. This suggests that filamentation should increase the number of overlaps within a suspension, thereby promoting network formation. Together, our approach provided a simple, controlled culturing method to modulate the cellular aspect ratio distribution of bacterial suspensions.

2.2 Micro-scale aggregation is enhanced by filamentation at intermediate bacterial concentrations.

Upon sedimentation, stationary phase dilute suspensions of *C. denitrificans* form space-spanning networks. These networks are interconnected and possess structural properties akin to a colloidal gel [27] (Fig.2a). Unlike prior reports of bacterial aggregates driven by depletion attraction or wastewater flocs, typified by dense cores with filaments protruding to the exterior, these networks were branched and possess a fractal-like diffuse growth structure [29]. We probe the dynamics of cluster-cluster aggregation at the microscale by loading NF and F cell suspensions into sealed glass capillaries (10 mm x 10 mm x 0.5 mm) and

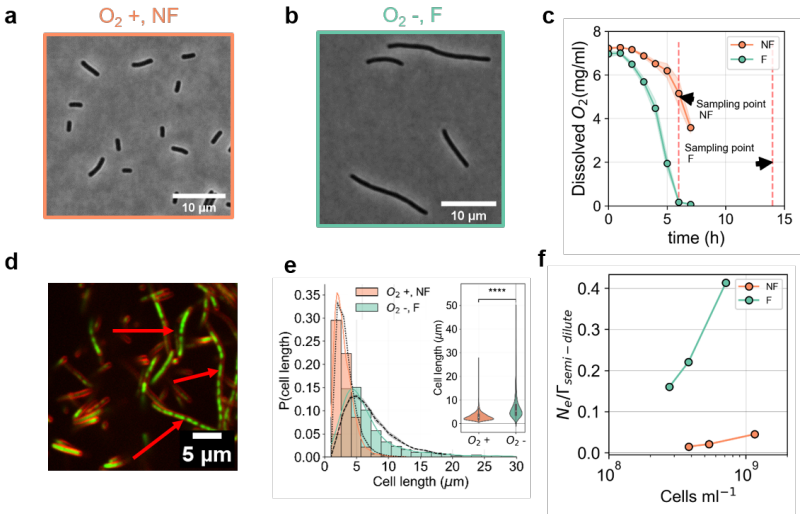

Fig. 1 Filamentation can be tuned by controlling oxygen concentration (**a, b**) Representative phase contrast images of *C. denitrificans* grown in O_2+ (a) and O_2- (b) conditions. (**c**) Dissolved O_2 concentrations in the O_2+ and O_2- culture vessels during cell growth. Presented are the mean of 3 biological replicates plus minus the standard deviation. (**d**) Representative confocal laser scanning microscopy image of F *C. denitrificans*. The white arrows highlight the multi-nucleated filamentous structure, whereby multiple cell cytoplasms (green- labeled with Syto 9) are encased within a continuous cell membrane (red - labeled with SynaptoRed C2). (**e**) Cell length probability distributions for the NF (n = 10117) and F (n = 3570) cell suspensions. Cell lengths were calculated from phase contrast microscopy images reported in a and b. (**f**) The effective number density, μ_e, of cell suspensions normalised by the theoretical semi-dilute limit, $\Gamma_{semi-dilute}$, for the different cell concentrations (cells ml^{-1}). The Mann-Whitney U test was used for the statistical analyses. **** denotes P $<$ 0.0001

observe the sedimentation of the suspensions using optical microscopy over a 2-hour period, estimated using the theoretical terminal velocity range for the cells (0.06 - 0.11 μms^{-1}; Supplementary Fig.2). Image segmentation is applied to obtain the packing fraction dependence on height and cluster number evolution of the networks as they form (Supplementary Fig.3). After this period of sedimentation, the suspensions form aggregated network-like structures on the surface of the capillary (Fig.2a). We compare the three suspension number densities that reside within the semi-dilute regime from (Fig.1f) for the NF and F phenotype.

The structural and dynamic properties of these bacterial networks are correlated with bacterial concentration and the filamentation phenotype. In sedimented suspensions of both phenotypes, the cells within these networks are connected via tip-tip and tip-body contacts and exhibit branch-like structures (red arrows highlight the contact modes in Supplementary Fig.4 a, b). Increasing the initial concentration of cells increased the rate of network formation for both phenotypes (Supplementary Fig.5). At the lowest number densities, both the NF and F cells settled on the bottom surface as quasi-2-D clusters. In this

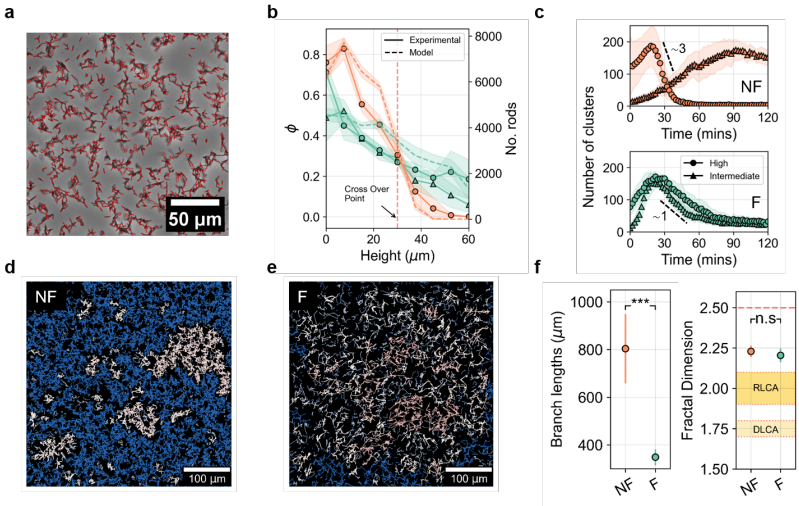

Fig. 2 ***C.denitrificans*** **forms bioflocculated gel-like structures on the microscale** (**a**). Representative micrograph of the bioflocculated network structure formed by the low number density NF phenotype upon sedimentation after two hours; the slice presented is taken at the glass capillaries bottom surface. Red lines indicate connected network structures. (**b**) Packing fraction dependence upon the height of the bacterial suspension. The NF phenotype is indicated by the orange lines and the F phenotype is indicated by the green lines. Experimental data is indicated by the solid lines, whilst the results from the model are represented by the dashed lines of the respective phenotype colors. The red dashed line indicated the "cross-over point" at which clustering data were analysed. Presented are the mean and standard deviation from at least 3 biological replicates. (**c**) Respective cluster numbers for the NF and F phenotypes at intermediate and high initial cell number densities. Presented are the mean and standard deviation from at least 3 biological replicates.(**d**) Representative micrograph of the NF bacterial networks acquired 30 μm above the bottom surface. Connected clusters are indicated by the color coding. (**e**) Representative slice of the F bacterial networks taken 30 μm above the bottom surface. Connected clusters are indicated by color coding. (**f**) Branch lengths of the bacterial gels were calculated from CLSM images taken of high-number density bacterial networks formed after 2 hours. The fractal dimension of the bacterial networks formed after 2 hours, featured are the reaction-limited aggregation (RLA) and diffusion-limited aggregation (DLA) regions. Plotted are the mean and the standard deviation from at least 3 biological replicates. Paired t-tests were performed for statistical analyses. n.s denotes non significant, *** denotes $P < 0.001$

case, the settling rate was independent of filamentation (Supplementary Fig.5). At the intermediate number densities, the F phenotype significantly increased the rate of network formation in comparison to the NF phenotype (Supplementary Fig.5, red dashed lines). The F networks increased in density until plateauing at $\phi \approx 0.4$ after ≈ 60 mins. Here, we see the emergence of layered 3-D connected structures where the packing fraction decreases with increasing height. This relationship is stronger in the NF phenotype (steeper slope in Fig.2b), which is bound by a higher and lower density of cells at the base and top, respectively. The weaker but linear relationship (shallower slope Fig.2b) exhibited by the F phenotype points to the presence of a space-spanning network, which, contrary to the NF phenotype, also forms at intermediate cell

concentration (Fig.2b, triangles). This behaviour is reproduced in Langevin simulations in sedimenting colloidal-rod suspensions (see methods).

The dynamical behaviour of the respective networks formed by the F and NF phenotype can be investigated further by probing the time evolution of the number of clusters. To allow for a valid comparison, we performed this analysis at a height (30 μm) where the volume fraction of the two systems crossover and are equal (Fig.2b). Cluster formation in both systems occurred via three distinct stages typically associated with hierarchical self-assembly: 1) cells collide and stick together to form small clusters; 2) these small clusters collide together to form larger clusters; 3) clustering together of these large clusters to form one (or very few) connected cluster(s). Stages 1) and 2) are separated by the peak in the number of clusters, which occurs at around 30 mins in the F phenotype at both intermediate and high cell concentration (Fig.2c, lower panel). Likewise for the NF phenotype at high concentration, however, at intermediate concentration, this transition approximately 60 mins later, suggesting that the dynamics of network formation are more strongly dependent on concentration for NF cells. Furthermore, the cluster-cluster aggregation in NF phenotype occurs more rapidly (exponent of 3) than the F phenotype (exponent of 1) at high concentration, suggesting greater connectivity, as indicated by the growth in the largest cluster size with time (Supplementary Fig. 6).

To probe the microstructure of the networks in more detail, we employed CLSM to compute the total number of branch lengths in each of the connected clusters and their fractal dimension. Surprisingly, clusters are on average shorter in the F phenotype (Fig.2f, compare 348.58 μm$\pm$33.92 vs 803.79 μm$\pm$145.60). The fractal dimension of the networks was invariant of phenotype: the F networks had a fractal dimension of 2.20 $\pm$0.04 compared to the NF networks, which were 2.23 $\pm$0.03 (Fig.3f). The fractal values placed the F and NF networks between the characteristic range of reaction-limited fractal networks (1.9 - 2.1) and below the percolation transition of 2.5. Furthermore, this value range indicates a flow-induced rearrangement of the clusters as they sedimented.

2.3 Bacterial networks relax via three characteristic modes

Bacterial networks can transmit stress through their structure, an indication of cohesion between the constituent elements, which confers structural and mechanical integrity. This is typical of colloidal gels. To test the mechanical response, we inverted the capillaries, containing bacterial networks on the capillary floor (after 2 hours), to subject the networks to gravitational stress. The deformation of the networks was observed for 2 hours and quantified using the normalised volume fraction, $\phi_{norm} = \phi_t/\phi_{t=0}$, where ϕ_t is the volume fraction at t, and $\phi_{t=0}$ is the volume fraction at the start of the reversal experiment. Bacterial networks have four time-dependent deformation modes: cluster-cluster deconstruction, where individual clusters gradually break away

from the collective structure (type I), delamination of the entire network structure originating at the base layer (type II), network relaxation, where the network remains fully intact but relaxes slowly with time until a plateau is reached (type III) and fragmented yielding, where sub-regions of the network fracture and break away from neighboring network regions which remain intact and surface attached, indicating viscoelastic solid behaviour (type IV) (Supplementary videos 1 and 2). Networks composed of F cells yield through type I cluster-wise detachment with a rate of $\sim -0.03\text{min}^{-1}$ (Fig.3a, dashed line) over a 60-minute period (Fig.3a). Upon interrogation of the final structure (on the capillary ceiling), we see a layer of surface-attached cells and tufts, indicating that network cohesion was the strength limiting factor (Supplementary Fig.9). In contrast, the NF networks initially exhibited type III behaviour; however, after ≈ 60 mins, a subset of the networks (33%, Supplementary Fig. 8) experienced fragmented type IV yielding from the ceiling (Fig. 3b, dashed line) (Supplementary video 3).

These contrasting deformation traits suggest that the F phenotype produces weaker bacterial networks in comparison to the NF cells. The elasticity of colloidal gels is dependent on the number of contacts between the colloidal particles and the colloidal interaction strength [30]. To gain insight into the number of contacts, we performed a network analysis on the final configuration generated in our Langevin dynamics simulations. The topology of resulting contact maps (Fig.3d, e) revealed structural differences with the F phenotype networks exhibiting fewer contacts ($9.50\text{x}10^5 \pm 0.06$ vs $14.93\text{x}10^5 \pm 0.06$) and shorter path lengths (9.77 ± 0.28 vs 15.40 ± 0.18) through the network (Fig.3f) in agreement with the CLSM branch length analysis (Fig.2d, e). To obtain a comparative quantification for the cohesion strength of the cells, we used the microbial adhesion to hydrocarbon assay (Methods). The NF cells had a significantly higher hydrophobicity than the F cells (29.17 %$\pm$2.97 vs. 1.99 %$\pm$1.41)(Fig.3c). Together, these data suggest that the filamentous phenotype produces networks with a reduced number of contacts and hydrophobicity that are mechanically weaker as a result.

2.4 Enzymatic treatment of bacterial gels enhances network strength

The relative cohesive strength of bacterial networks can be tuned by modifying cell surface hydrophobicity using glycoside hydrolase enzymes, known to degrade bacterial polysaccharides. The presence of polysaccharides on the cell surface can influence surface hydrophobicity, creating a hydrophilic interface [31, 32]. To probe the influence of cell surface polysaccharides on the network deformation, we treated the cell suspensions with α-amylase, which hydrolyses α-1,4 linkages, and cellulase, which hydrolyses β-1,4 linkages. Phase contrast microscopy reveals that treatment with α-amylase degrades the polysaccharide components on the cell envelope of *C. denitrificans*, which causes a significant loss in cell viability (Supplementary Fig.9, 10). Treatment with cellulase on the other hand had little effect on the integrity of the cell envelope and

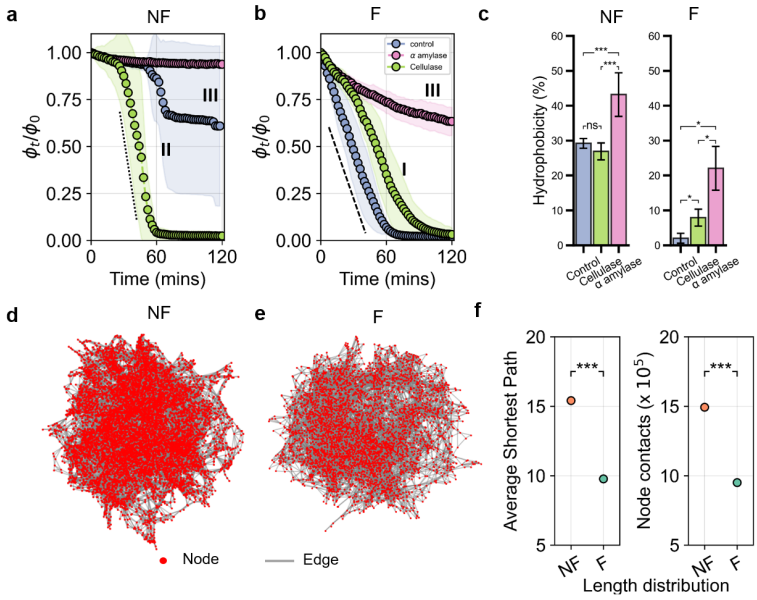

Fig. 3 Connectivity and network strength vary as a function of filamentation and cell surface hydrophobicity (**a, b**) Normalised change in packing fraction from 30μm above the base of the bacterial networks for F and NF cells respectively. The error bar for the control NF cells increases at t = 60 mins due to the emergence of type IV yielding in a subset of the bacterial networks (33%). The data presented are the mean and standard deviation from at least 3 biological replicates each with 5 different fields of view. (**c**) The cell surface hydrophobicity of F and NF cell suspensions treated with α-amylase and cellulase enzymes, the control are untreated cells, and the data presented are the mean and standard deviation from at least 3 biological replicates. (**d, e**) Network analysis of F (d) and NF (e) cell length distribution from the model. The red dots indicate nodes, and the grey lines indicate the edges of the network graph. (**f**) The average network path and the number of node contacts are calculated from the network graphs. The data presented are the average and standard deviation from 3 simulation runs. Paired t-tests were performed for statistical analyses. n.s denotes non significant, * denotes P $<$ 0.05, *** denotes P $<$ 0.001, **** denotes denotes P $<$ 0.0001

cell viability. Cells of the filamentous phenotype are less hydrophobic than their nonfilamentous counterpart. In both systems, treatment with α-amylase led to a large increase in cell-surface hydrophobicity, but this increase was more significant when the cells were F (from 1.99%$\pm$1.41 to 22.01 %$\pm$6.26 and from 29.17%$\pm$2.97 to 43.15 %$\pm$0.42, respectively). Cellulase treatment did not significantly affect NF cells; however, it significantly increased the cell surface hydrophobicity of the F cells (7.90 %$\pm$2.42), though in comparison to α-amylase the fold change was minor, and no cell morphological changes were observed (Fig.3c).

Enzymatic modification of cell surface hydrophobicity induces transitions to the bacterial network yielding modes. The F and NF bacterial networks treated with α-amylase transitioned from type I and type IV behaviours, respectively, to a type III extensional deformation mode. After a two-hour

period, the respective normalised volume fractions ϕ_{norm} for the F and NF cells were 0.63±0.07 and 0.95±0.07 (Fig.4c). While cellulase treatment did not induce any deformation-mode changes, it did affect the time dependence of the respective deformation modes. The F cellulase-treated cells remained type I; however, the treatment induced a lag-time of ≈ 25 mins in the onset of type I behavior compared to the control. In cellulase-treated NF networks, the lag time before the type II delamination event, which displayed a characteristic $\frac{d\phi_{norm}}{dt}$ gradient of -0.06min^{-1} was reduced from 60 mins to 30 mins (Fig.3b). This delamination mode indicates that surface/network adhesion was the strength limiting interaction, as the networks remained intact. α-treated cells for both the F and NF networks had type III deformation. Both networks remained intact throughout the observation period, indicating increased cell-cell and cell-surface cohesion.

2.5 Filamentation reduces the collapse rate of bacterial structures

At the macroscale, during sedimentation of *C. denitrificans*, the suspensions undergo a rapid collapse after an initial quiescent phase, followed by a slower compaction (Fig.4a). While in the previous sections, we interrogate the microscopic structure and dynamics of *C. denitrificans* suspensions during sedimentation, here we adopt a macroscopic approach by tracking the dynamics of the interface that emerges between the concentrated and supernatant phases (Fig.4a, see Methods). We monitored the time evolution of this interface using a horizontal imaging platform, in which a transmission image of the sample (17 cm x 0.5 cm x 1 cm) is obtained by a camera lens (Methods). We compared the three suspension number densities that resided within the semi-dilute regime reported in Fig.1f for the F and NF phenotype.

During sedimentation, we see three distinct dynamical regimes in both phenotypes: 1) an initial quiescent phase; 2) rapid collapse; and 3) slow compaction. Stage 1 is defined by the homogeneous intensity in the image, which corresponds to a homogeneous distribution of the cells as a function of height. During stage 2, cell flocculation gives rise to a coarser image intensity (Fig.4a, b, I), and in stage 3 a clear interface emerges that falls more slowly with time. It is clear, however, that the dynamics of sedimentation are very different in the two phenotypes.

In the NF phenotype, we see the emergence of a diffuse interface that then falls linearly with time, suggesting that discrete flocs form and sediment individually (Fig.4a, II). These flocs deposited on the floor of the cuvette resulting in a dense compact phase after ≈ 40 mins (Fig.4a, III and dashed red line). In the F phenotype, however, we see the emergence of a clear interface after ≈ 20 mins that also falls linearly with time. The emergence of this well-defined interface points to a sweeping regime in which the hierarchical self-assembly of interacting clusters results in collective settling, i.e., one connected cluster (Fig.4b, dashed red line). The influence of the initial number density on these dynamics is subtle. For example, there is no clear trend on the quiescent

time t_q in the F phenotype, yet there is a decreasing trend in the NF phenotype (Fig.4c). Likewise, there is no clear trend in the sedimentation velocity, u_{sed} of the NF phenotype, yet there is a decreasing trend in the F phenotype (Fig.4f).

We define the "gel point" in our suspensions as the height at which the sharp supernatant interface emerges during sedimentation. This also corresponds to the transition point between regime 1 and regime 2 (4a, b, red dashed line) and is significantly higher in the F phenotype (12.42 mm $\pm$0.27 vs 3.42 mm $\pm$0.30; Supplementary Fig.11). After the "gel point", the height of both systems decays as a stretched exponential. Here, the gravitational stress exceeds the network's compressive yield strength, and the bacterial networks exhibit compaction behaviour analogous to a colloidal gel [33]. The smaller decrease in height in the initial gel point of the F suspension (46.2%$\pm$1.1 vs 87.9%$\pm$2.4) points to a network less prone to compaction (add fig).

More insight into cluster dynamics during sedimentation can be gained by quantifying the horizontally averaged normalised standard deviation in intensity (σ_I) with the height, h of the sample through time, t (Methods). The size of the fluctuations is reflected in σ_I and indicative of the rearrangement dynamics of the suspension during sedimentation. The higher fluctuations in the NF suspension point to faster rearrangement dynamics of clusters compared to the F suspension (Fig.4d). Upon the formation of the condensed phase, the system dynamics slowed for both the NF and F phenotypes, and a high variance interface formed between the bacterial phase and supernatant, indicating the sharp meniscus, confirming the formation of an interconnected structured (Fig.4d, e, red arrow).

3 Discussion and Conclusion

Our study elucidates the contribution of cellular aspect ratios to bacterial network self-assembly and subsequent 3D network properties, demonstrating an approach to manipulate bioflocculation. We showed how the height-dependent packing fraction and spatial properties could be controlled by modulating cell length and concentration. Furthermore, the dynamics of the bacterial networks could be tuned as a function of cell length and cell surface hydrophobicity. Using Langevin dynamics simulations, we demonstrated that the properties of bacterial network formation and properties can be captured using experimentally obtained cell length distributions and approximated interaction potentials. The behaviour of this bacterial system echoes the principles foundational to colloidal network formation.

Nano and micro biogel assemblies take advantage of the inherent biological traits of their sub-units to form supra networks. Our work took inspiration from biofilm self-assembly and applied passive sedimentation and bioflocculation to create bacterial networks. We varied the dissolved O_2 concentration, in order to tune the aspect ratio distribution of the bacterial network sub-units. In abiotic systems such as injectable high aspect ratio scaffolds the scaffold height dependence is routinely controlled by varying sub-unit aspect

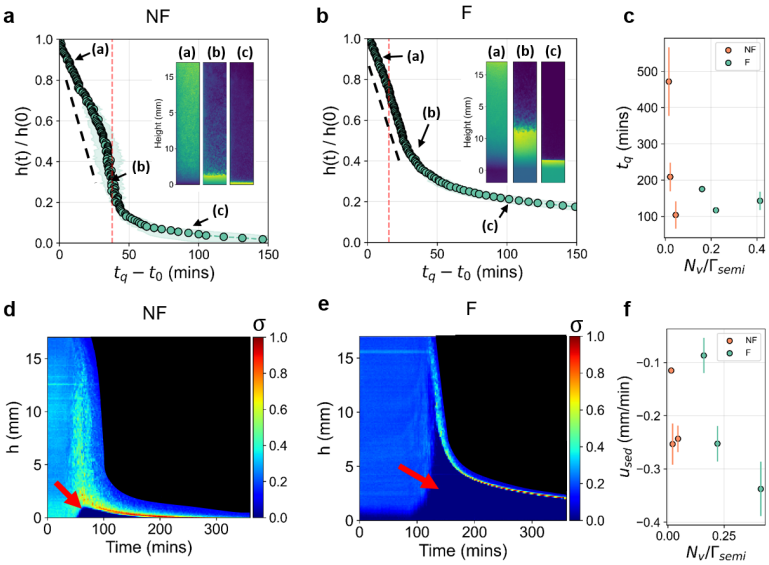

Fig. 4 Bacterial suspensions display collapsing gel behaviour upon phase separation (**a, b**) Height as a function of time for the NF and F bacteria suspensions after an initial lag time t_q. $h(t)$ displays a linear relationship (I, black dashed line) with time before the meniscus is formed (II, red dashed line). The meniscus collapsed following a stretched exponential relationship with time (III). Insets (I, II and III) are representative micrographs of the cuvette and bacterial suspension. The concentrated regime displays a collapsing gel dynamic. (**c**) The quiescence time, t_q is plotted as a function of respective number densities for both the NF and F bacterial suspensions, displayed are the mean and the standard deviation from at least 3 biological replicates. (**d, e**) Dependence of the normalised standard deviation in intensity $\sigma(h, t)$ with height, h and time, t for the NF and F suspensions. The color bars indicate the scale of the normalised standard deviation. The gel point and collapse are highlighted with red arrows. The black region indicates the cell void supernatant. (**f**) Sedimentation speed of the NF and F bacterial suspensions was measured from the linear portion of the collapse curve from (a and b) as a function of initial suspension number density. Displayed is the mean and standard deviation from at least 3 biological replicates.

ratio [34]. However abiotic rod systems typically require laborious synthesis approaches, and cannot self-replicate, limiting scalability [34, 35]. Bacterial network systems are intrinsically self-replicating and inherently biocompatible where simple biologically derived approaches can be applied to tune network formation. However, bacterial cell size is polydisperse conforming to a log-normal distribution, potentially limiting precise control over the conformation of these structures.

Our results show that the formation of intermediate number density 3D networks could be enhanced by inducing filamentation. In non-interacting hard rod systems, the fat-tails of the log-normal distribution reduce the isotropic-nematic phase boundary [36]; therefore, we speculate that the percolation boundary in our bacterial system is reduced as a function of filamentation. Our combined experimental and computational analysis sheds light on the role

bacterial aspect ratio distribution plays in reducing plateau packing density of basal network regions (< 30 μm height), reducing cluster size, and reducing network connectivity. Bacterial aggregates are typically compact clusters or flocs formed due to the expression of exopolymers or are artificially induced by depletants [37, 38]. Whilst hydrophilic sheathed filamented bacteria form network pellicles on the liquid-air interface [39]. Our findings indicate that networks formed via bioflocculation are an additional cluster type found in submerged systems.

The emergence of mechanical stability in abiotic colloidal networks is increasingly attributed to the percolation of isostatic and glassy clusters [30, 40]. Colloidal network mechanical stability is attributed to three predominant factors; cluster density, cluster connectivity, and bond rigidity. Our results indicate that the mechanical behavior of bacterial networks under gravitational stress transitions as a function of cluster connectivity and cell surface hydrophobicity, a relative measure frequently correlated to cohesion strength in bacterial aggregates [41]. Cell filamentation reduced network connectivity, whilst lowering cell surface hydrophobicity, resulting in cluster-cluster yielding. Colloidal networks are routinely stabilised via the surface treatment of composing units, using techniques such as hydrophobation [42]. Our findings indicate that bacterial network mechanical behaviour can be tuned with hydrophobation using glycoside hydrolase enzymes.

To gain more insight into our experimental observations, we performed Langevin Dynamics simulations of sedimenting colloidal-rods; the length of which were determined by the experimental log-normal cell length distributions (Fig.1e). We anticipate that our experimental approach to self-assembly and modeling early-stage bacterial network structures could apply to other bacterial species, although, variations in cell length distribution and interaction strength, which are dependent on cell surface biopolymers are likely to produce different compaction and formation dynamics.

Exploring control parameters of bacterial network formation by tuning filamentation and applying enzymatic treatments offers an intriguing avenue for passively fabricating living material network structures guided by sedimentation. Contemporary fabrication approaches use homogeneously distributed cell suspensions, limiting the potential benefits that can arise from structured bacterial communities [43]. If combined with compendial encapsulation approaches, a sedimentation network formation approach could potentially enable large-surface area manufacturing of active, structured living materials. For example, increased focus is being placed on living hydrogels for the sequestration of organic compounds [44]. Furthermore, applying our approach to induce and tune network formation of electrogenic bacteria, before hydrogel crosslinking could enhance power output, as electron shuttling and network percolation would theoretically be enhanced [45].

In conclusion, this work opens up possibilities for advancing bacterial modeling and biotechnological applications by considering realistic cell length distributions, providing valuable insights into settling behavior and bacterial

network formation. Moreover, the potential to engineer living network structures through enzymatic treatment and hydrogel encapsulation holds promise for creating innovative surface coatings with environmental and industrial significance. Ultimately, these findings bear relevance to real-world environments such as bioreactors and wastewater treatment plants, where flocculation and settling are integral parts of the process. By exploiting the lessons from colloidal physics and cellular morphological control, we can optimize the design of biological materials and systems, promising advancements in a wide range of biotechnological applications.

4 Methods

4.1 Bacterial Culture

Experiments were performed using *Comammonas denitrificans* 123 (ATCC 700936). *Comammonas denitrificans* suspensions were prepared by inoculating 5 ml tryptic soy broth (TSB) with cells from glycerol cryo stocks and incubated at 30$\circ$ C with 180 rpm shaking. Dissolved oxygen conditions were controlled by modulating the head space in the culture vessels. To create O_2- conditions 14 ml culture tubes were used, which provided a 1.8x headspace. O_2+ conditions were created by using 50 ml falcon tubes, which provided a 9x headspace.

4.2 Cell length distributions

To measure cell lengths, cell cultures were grown to OD = 1.0. 2 μL of culture was transferred to a 1.5 % agarose pad which was covered with a No 1.5 coverslip. Imaging was performed using a Nikon Ti inverted microscope (Nikon, Japan) with a digital camera. Bacterial cells were imaged in phase contrast mode using a 63x oil immersion objective. Three biological replicates were performed, and up to 15 fields of view (147 μm x 147 μm) were acquired per biological replicate. The cell length was quantified using compendial image segmentation methods, using binarisation, and then the skeletonization function in Fiji ImageJ. The images were padded and cells that were at the edge of each frame were removed from the analysis.

4.3 O_2 concentration measurements

O_2 concentration during cell culture was measured using an optical oxygen measurement system (PreSens Oxygen Meter, PreSens, Germany). Oxygen-sensitive probe spots adhered to the inside of the relevant culture vessels with manufacturer-provided adhesive. Vessels were then sterilised using Isopropanol. The sensor was calibrated using oxygen-saturated water and zeroed with 300 mM sodium sulfite. Culture vessels were filled with 5 ml TSB media and inoculated at a 100:1 ratio from overnight cultures. Oxygen concentrations were measured every hour for 8 hours. For each condition, 4 biological replicates were used.

4.4 Cell surface hydrophobicity measurement

We measured the comparative cell surface hydrophobicity (CSH) of the cell suspensions by performing the microbial adhesion to hydrocarbon (MATH) assay [46]. Bacterial cultures were grown to an OD of 1 as previously described. Upon sampling, 1 ml of the culture was centrifuged (2700 rcf) for 2 minutes and cleaned 3 times with fresh media. Resuspended cells were then diluted to an OD_{600} of 0.5 in a 5 ml test tube. 4 ml of cell suspension was mixed with 1 ml of hexadecane (Sigma Aldrich) and vortexed at full speed for 2 mins. Mixed suspensions were then left to phase separate for 30 minutes. After a syringe with a needle tip was used to collect 1 ml of cell suspension from the aqueous phase. The OD of this suspension was then measured. The percentage hydrophobicity was calculated as $CSH_{cell} = \frac{OD_{600initial} - OD_{600final}}{OD_{600initial}}$. Low % values indicate hydrophilicity, whilst high % values indicate hydrophobicity.

4.5 Horizontal imaging setup

We determined the sedimentation behaviour and collapse of the meniscus using digital imaging. Samples were prepared to the relevant number density and homogenised using gentle vortexing before transfer into 2.5 mm x 10 mm x 20 mm plastic cuvettes for time-lapse observation at 21$\circ$ C. The imaging platform comprised a CMOS camera (SVS-Vistek, Vision Systems LLC) with a 35 mm lens (HF3514V-2, Myutron). An LED panel provided illumination with a diffuser and images were acquired in transmission mode. Images were acquired every 2 minutes for at least 300 mins. To obtain the sedimentation behaviour and collapse of the meniscus, image analysis was performed. The sedimentation dynamics of each bacterial suspension were calculated by tracking the intensity profile through the height of the cuvette. The cuvette was split into horizontal regions of interest across the central 2mm of the cuvette with a height of 5 pixels. The intensity in these regions was tracked in time, when the intensity dropped below a threshold value the region was deemed to be clear of cells. The time taken for each region to be void of cells was measured for each region of interest which enabled us to track the height of the suspension before a clear meniscus had formed. The quiescence time, t_q was calculated as the time taken for the top region of interest of the cuvette to become void of cells. The sedimentation velocity, u_{sed} was calculated as the gradient from the linear portion of the $h(t)$ curve until the meniscus formed for each concentration and phenotype.

The emergence of the meniscus was characterised by a sharply contrasting interface between the supernatant and the sample. The emergence of the meniscus was calculated by tracking the vertical line profile of the central 2 mm region of each frame. A meniscus was deemed to have formed when the intensity gradient exceeded a threshold value that corresponded to the interface between the supernatant and dense bacterial phase. The height of the meniscus interface was then tracked with time. To calculate the standard deviation in intensity with time the raw images were split into regions of interest

of 4 pixels high and across the central 2 mm of the curvette. The standard deviation in intensity was then calculated for each of these regions across the period of observation.

4.6 Sedimentation experiments and reversal

For each experiment cell suspensions were grown to OD = 1.0, 1 ml of this culture was aliquoted into a 1.5 ml centrifuge tube. Cells were gently centrifuged for 90 seconds at 2700 rcf, the supernatant was discarded and cells were resuspended in 1 ml, 0.5 ml, and 0.25 ml of media. For experiments involving enzyme treatment, the cells were resuspended either 100 mg/ml α-amylase (Sigma Alderich, Switzerland) or 125 mg/ml cellulase (Sigma Alderich, Switzerland), re-suspended and incubated without shaking at 30 $\circ$C for 2 hours. Cells were then vortexed for 90 seconds to re-suspend and create a well-dispersed suspension. We ran control experiments to confirm that centrifugation and vortexing had a negligible effect on network formation.

Gel network formation through sedimentation was performed on an inverted microscope (magnification 20x + 1.5x zoom) with a piezostage (Nikon Ti, Nikon, Japan). The imaging cell (10 mm x 10 mm x 500 μm) was created by layering 2 geneframes (Sigma Alderich, Switzerland). 54 μL of polydisperse cell culture was pipetted into the imaging area and sealed using a No. 1.5 coverslip. The slide was immediately transferred to the microscope, and imaging commenced no later than 5 mins after sample preparation. Imaging was performed using brightfield mode with Koeller illumination condition with the condenser 2/3 closed. Z stacks of 10 μm increment from the bottom surface of the imaging area to 90 mum into the imaging volume were acquired every 2 minutes for 120 mins. 5 fields of view (441 μm x 441μm) were acquired for each experimental condition, and at least 3 biological replicates were tested. Reversal experiments followed the same sedimentation procedures; however, after 2 hours of sedimentation, the imaging cell was inverted. Z stacks were then acquired from the top of the imaging arena to 90 μm depth.

4.7 Effective Number density calculations

The effective number density of the cellular suspensions was calculated using the measured cell length distributions for the NF and F cells and their respective cell concentrations ($cellsml^{-1}$) from the flow cytometry measurements. The number density for rods with a defined length can be calculated as $V = \frac{N}{V}$ where N is the number of rods and V is the sample volume. However, for suspensions of rods with a length distribution, the effective number density is calculated as $V_e = \frac{N_e}{V} = \frac{\sum_{i=1}^{l_{\max}} (\frac{V_{\text{bact}}}{V_{\text{cyl}_i}})}{V}$ [47]. In the equation, N_e represents the effective number of cells, $l_{\max}$ is the longest cell length, V_{bact} is the volume of cells in the sample, ϕ_i is the volume fraction of cells with length i, and $V_{\text{cyl}i}$ is the volume of a single cell with length i. We estimate $V\text{cyl}_i$ using a spherocylindrical geometry.

4.8 Langevin simulations

We model our non-growing bacterial cells as rigid straight chains of connected beads, with neighbouring beads separated by a distance σ. The length of each rod, in units of beads (or σ), is drawn from a log-normal distribution corresponding to the "filamentous" (mean = 1.848σ, sd = 0.574σ) and "nonfilamentous" (mean = 1.050σ, sd = 0.469σ) phenotypes in Fig.1e.

Beads interact with beads on other rods via a cut-and-shifted Lennard-Jones (LJ) potential,

$$U = 4\epsilon \left[\left(\frac{\sigma}{r}\right)^{12} - \left(\frac{\sigma}{r}\right)^{6} - U_c \right], \tag{1}$$

where ϵ governs the strength of the interaction in units of $k_B T$, σ is the bead diameter, and $U_c = (\sigma/r_c)^{12} - (\sigma/r_c)^6$ ensures that the potential is equal to zero at the cut-off distance r_c. For equilibrium runs, $r_c = 2^{1/6}\sigma$, corresponding to the Weeks-Chandler-Anderson (WCA) potential. Otherwise $\epsilon = 50$ and $r_c = 1.4\sigma$ is used to model strongly attractive and short-ranged interactions between the beads.

We use the Large-scale Atomic/Molecular Massively Parallel Simulator (LAMMPS) [48] to perform Langevin Dynamics (LD) simulations of our sedimenting colloidal rods . The time evolution of each bead is governed by the Langevin equation,

$$m\frac{d^2\mathbf{r}}{dt^2} = -\gamma\frac{d\mathbf{r}}{dt} - \nabla U + \sqrt{2k_B T\gamma}\eta(t) + \mathbf{F}_g, \tag{2}$$

where U is the potential energy on the bead resulting from the sum of interactions with all other beads in the system, m is the mass of the bead, γ is the friction coefficient, $\mathbf{F}_g$ is the force due to gravity, and η is a white noise term with zero mean and variance given by

$$\langle \eta_\alpha(t)\eta_\beta(t')\rangle = \delta_{\alpha\beta}\delta(t-t') \tag{3}$$

along each Cartesian components. This equation is integrated using a velocity-Verlet scheme. Here, energy is set in units of $k_B T$, where k_B is the Boltzmann constant and T is the temperature. Furthermore, given that we are interested in bacteria, we set our characteristic lengthscale σ to be 1μm.

In our simulations, we consider the time τ_D for a bead to diffuse its own length, σ, as the natural unit of time, which is related to the diffusion coefficient D of a colloidal particle through $\tau_D = \frac{\sigma^2}{D}$. Using the Stokes-Einstein relation $D = \frac{k_B T}{\gamma}$, we can related the diffusion coefficient D to the friction coefficient γ, which in turn relates to the dynamic viscosity μ through $\gamma = 3\pi\mu\sigma$.

We simulated our bacterial suspensions at volume fractions $\phi = 0.015$. Initial configurations for any given system were set up by filling a simulation box, $80 \times 80 \times 160\sigma^3$, with rods drawn from either the F or NF distribution. Rods

were constructed by placing the first bead of each rod at a random location in the box and sequentially adding extra beads along the x direction at distances σ until the length of the rod matched that drawn from the distribution.

A 3-step equilibration of this initial configuration was then performed. In the first step, particle overlap resulting from the initial configuration was removed by "relaxing" the system using a soft cosine potential for $5 \times 10^2\tau$. Then, in the second step, the system was allowed to "relax" more by switching to a WCA potential for a further $2 \times 10^2\tau$. Finally, we increased the timestep from 5×10^{-4} to $5 \times 10^{-3}\tau$ for a further $10^4\tau$ to distribute the bacteria evenly throughout the simulation box.

For both F and NF suspensions, four different initial configurations (resulting from different input random seeds) were relaxed in this three-step process to generate 4 equilibrated configurations. These 4 equilibrated configurations were then used as the starting configuration for simulated sedimentation runs of duration $10^4\tau$. To simulate gravity, a downward force ($\mathbf{F}_g$) of -0.1 ϵ/k_BT was applied to each bead. Thus 4 simulations were performed, each with a different starting configuration and random seed for the Langevin noise.

To quantify the network features from simulation data, we proceed as follows. First, a network is constructed from a configuration (simulation snapshot) by identifying rods as nodes, and by adding an edge between each pair of rods which is below a threshold distance (equal to 1.2σ, note the distance between two rods is computed as the minimum between the pairwise distance of any pair of beads belonging to the two different rods). Then, we characterise the connectivity of each network by computing: (i) the total number of connections (or edges), and (ii) the average shortest path between a node pair. The analysis has been performed by using the python library NetworkX [49]. Values reported in the main text are then averaged over different configurations, for each condition.

Acknowledgments. The authors would like to thank Dr. Jonasz Slomka for the valuable discussions. The authors acknowledge support from SNSF PRIMA grant 179834 (to E.S.) and MSCA individual fellowship grant 101033169 (to S.C.). G.M would like to thank NBIC/BBSRC/UKRI (Grant No. BB/R012415/1) for financial support.

Competing interests. The authors declare no competing interests.

References

[1] Flemming, H.-C., Wingender, J., Szewzyk, U., Steinberg, P., Rice, S., Kjelleberg, S.: Biofilms: An emergent form of bacterial life. Nature Reviews Microbiology **14**, 563–575 (2016). https://doi.org/10.1038/nrmicro.2016.94

[2] Dragoš, A., Kiesewalter, H., Martin-Pohle, M., Hsu, C.-Y., Hartmann, R., Wechsler, T., Eriksen, C., Brix, S., Drescher, K., Stanley-Wall, N.,

Kümmerli, R., Kovács, : Division of labor during biofilm matrix production. Current biology : CB **28** (2018). https://doi.org/10.1016/j.cub.2018.04.046

[3] Schwartzman, J., Ebrahimi, A., Chadwick, G., Sato, Y., Roller, B., Orphan, V., cordero sanchez, o.x.: Bacterial growth in multicellular aggregates leads to the emergence of complex life cycles. Current Biology **32** (2022). https://doi.org/10.1016/j.cub.2022.06.011

[4] Sauer, K., Stoodley, P., Goeres, D., Hall-Stoodley, L., Burmølle, M., Stewart, P., Bjarnsholt, T.: The biofilm life cycle: expanding the conceptual model of biofilm formation. Nature Reviews Microbiology **20** (2022). https://doi.org/10.1038/s41579-022-00767-0

[5] Wang, B., Zhang, H., Yang, Y., Xu, M.: Diffusion and filamentous bacteria jointly govern the spatiotemporal process of sulfide removal in sediment microbial fuel cells. Chemical Engineering Journal **405**, 126680 (2021). https://doi.org/10.1016/j.cej.2020.126680

[6] Aqeel, H., Weissbrodt, D.G., Cerruti, M., Wolfaardt, G.M., Wilén, B.-M., Liss, S.N.: Drivers of bioaggregation from flocs to biofilms and granular sludge. Environ. Sci.: Water Res. Technol. **5**, 2072–2089 (2019). https://doi.org/10.1039/C9EW00450E

[7] Jeckel, H., Díaz-Pascual, F., Skinner, D.J., Song, B., Jiménez-Siebert, E., Strenger, K., Jelli, E., Vaidya, S., Dunkel, J., Drescher, K.: Shared biophysical mechanisms determine early biofilm architecture development across different bacterial species. PLOS Biology **20**(10), 1–14 (2022). https://doi.org/10.1371/journal.pbio.3001846

[8] Lattuada, M., Zaccone, A., Wu, H., Morbidelli, M.: Population-balance description of shear-induced clustering, gelation and suspension viscosity in sheared dlvo colloids. Soft Matter **12**, 5313–5324 (2016). https://doi.org/10.1039/C6SM01097K

[9] Turetta, L., Lattuada, M.: The role of hydrodynamic interactions on the aggregation kinetics of sedimenting colloidal particles. Soft Matter **18**, 1715–1730 (2022). https://doi.org/10.1039/D1SM01637G

[10] Karasz, D.C., Weaver, A.I., Buckley, D.H., Wilhelm, R.C.: Conditional filamentation as an adaptive trait of bacteria and its ecological significance in soils. Environmental Microbiology **24**(1), 1–17 (2022) https://sfamjournals.onlinelibrary.wiley.com/doi/pdf/10.1111/1462-2920.15871. https://doi.org/10.1111/1462-2920.15871

[11] Crabbé A., W.R.A.A.L.N.C.P.V.H.R. Leroy B.: Differential proteomics and physiology of pseudomonas putida kt2440 under filament-inducing

conditions. BMC Microbiology **12**(1) (2012). https://doi.org/10.1186/1471-2180-12-282

[12] Bos, J., Zhang, Q., Vyawahare, S., Rogers, E., Rosenberg, S.M., Austin, R.H.: Emergence of antibiotic resistance from multinucleated bacterial filaments. Proceedings of the National Academy of Sciences **112**(1), 178–183 (2015) https://www.pnas.org/content/112/1/178.full.pdf. https://doi.org/10.1073/pnas.1420702111

[13] Tran, T., Ali, M., Lee, D., Félix, M.-A., Luallen, R.: Bacterial filamentation as a mechanism for cell-to-cell spread within an animal host. Nature Communications **13**, 693 (2022). https://doi.org/10.1038/s41467-022-28297-6

[14] Moeller, J., Emge, P., Avalos, I., Kollmannsberger, P., Vogel, V.: Bacterial filamentation accelerates colonization of adhesive spots embedded in biopassive surfaces. New Journal of Physics **15** (2013). https://doi.org/10.1088/1367-2630/15/12/125016

[15] Seder-Colomina, M., Goubert, A., Lacroix, S., Morin, G., Ona-Nguema, G., Esposito, G., van Hullebusch, E., Pernelle, J.-J.: Moderate oxygen depletion as a factor favouring the filamentous growth of sphaerotilus natans. Antonie van Leeuwenhoek **107**, 1135–1144 (2015). https://doi.org/10.1007/s10482-015-0405-7

[16] Wucher, B.R., Bartlett, T.M., Hoyos, M., Papenfort, K., Persat, A., Nadell, C.D.: ¡i¿vibrio cholerae¡/i¿ filamentation promotes chitin surface attachment at the expense of competition in biofilms. Proceedings of the National Academy of Sciences **116**(28), 14216–14221 (2019) https://www.pnas.org/doi/pdf/10.1073/pnas.1819016116. https://doi.org/10.1073/pnas.1819016116

[17] Rouwhorst, J., Ness, C., Stoyanov, S., Zaccone, A., Schall, P.: Nonequilibrium continuous phase transition in colloidal gelation with short-range attraction. Nature Communications **11** (2020). https://doi.org/10.1038/s41467-020-17353-8

[18] Ruiz-Franco, J., Camerin, F., Gnan, N., Zaccarelli, E.: Tuning the rheological behavior of colloidal gels through competing interactions. Phys. Rev. Mater. **4**, 045601 (2020). https://doi.org/10.1103/PhysRevMaterials.4.045601

[19] Nabizadeh, M., Jamali, S.: Life and death of colloidal bonds control the rate-dependent rheology of gels. Nature Communications **12** (2021). https://doi.org/10.1038/s41467-021-24416-x

[20] Harich, R., Blythe, T.W., Hermes, M., Zaccarelli, E., Sederman, A.J.,

Gladden, L.F., Poon, W.C.K.: Gravitational collapse of depletion-induced colloidal gels. Soft Matter **12**, 4300–4308 (2016). https://doi.org/10.1039/C5SM02651B

[21] Andersson, S., Rajarao, G., Land, C., Dalhammar, G.: Biofilm formation and interactions of bacterial strains found in wastewater treatment systems. FEMS microbiology letters **283**, 83–90 (2008). https://doi.org/10.1111/j.1574-6968.2008.01149.x

[22] Hem, S., Wyrsch, E.R., Drigo, B., Baker, D.J., Charles, I.G., Donner, E., Jarocki, V.M., Djordjevic, S.P.: Genomic analysis of carbapenem-resistant ¡i¿comamonas¡/i¿ in water matrices: Implications for public health and wastewater treatments. Applied and Environmental Microbiology **88**(13), 00646–22 (2022) https://journals.asm.org/doi/pdf/10.1128/aem.00646-22. https://doi.org/10.1128/aem.00646-22

[23] Gumaelius, L., Magnusson, G., Pettersson, B., Dalhammar, G.: Comamonas denitrificans sp. nov., an efficient denitrifying bacterium isolated from activated sludge. International Journal of Systematic and Evolutionary Microbiology **51**(3), 999–1006 (2001). https://doi.org/10.1099/00207713-51-3-999

[24] Holenda, B., Domokos, E., Rédey, , Fazakas, J.: Dissolved oxygen control of the activated sludge wastewater treatment process using model predictive control. Computers Chemical Engineering **32**(6), 1270–1278 (2008). https://doi.org/10.1016/j.compchemeng.2007.06.008

[25] Hosoda, K., Matsuura, T., Suzuki, H., Yomo, T.: Origin of lognormal-like distributions with a common width in a growth and division process. Physical review. E, Statistical, nonlinear, and soft matter physics **83**, 031118 (2011). https://doi.org/10.1103/PhysRevE.83.031118

[26] Doi, M., Edwards, S.F.: The Theory of Polymer Dynamics. Clarendon Press, Oxford (1986)

[27] Solomon, M.J., Spicer, P.T.: Microstructural regimes of colloidal rod suspensions, gels, and glasses. Soft Matter **6**, 1391–1400 (2010). https://doi.org/10.1039/B918281K

[28] Saunders, A., Albertsen, M., Vollertsen, J., Nielsen, P.: The activated sludge ecosystem contains a core community of abundant organisms. The ISME journal **10** (2015). https://doi.org/10.1038/ismej.2015.117

[29] Dorken, G., Ferguson, G., French, C., Poon, W.: Aggregation by depletion attraction in cultures of bacteria producing exopolysaccharide. Journal of the Royal Society, Interface / the Royal Society **9**, 3490–502 (2012). https://doi.org/10.1098/rsif.2012.0498

[30] Whitaker, K., Varga, Z., Hsiao, L., Solomon, M., Swan, J., Furst, E.: Colloidal gel elasticity arises from the packing of locally glassy clusters. Nature Communications **10** (2019). https://doi.org/10.1038/s41467-019-10039-w

[31] Dertli, E., Mayer, M., Narbad, A.: Impact of the exopolysaccharide layer on biofilms, adhesion and resistance to stress in lactobacillus johnsonii fi9785. BMC microbiology **15**, 8 (2015). https://doi.org/10.1186/s12866-015-0347-2

[32] Kouzuma, A., Meng, X.-Y., Kimura, N., Hashimoto, K., Watanabe, K.: Disruption of the putative cell surface polysaccharide biosynthesis gene so3177 in ¡i¿shewanella oneidensis¡/i¿ mr-1 enhances adhesion to electrodes and current generation in microbial fuel cells. Applied and Environmental Microbiology **76**(13), 4151–4157 (2010) https://journals.asm.org/doi/pdf/10.1128/AEM.00117-10. https://doi.org/10.1128/AEM.00117-10

[33] Secchi, E., Buzzaccaro, S., Piazza, R.: Time-evolution scenarios for short-range depletion gels subjected to the gravitational stress. Soft Matter **10**, 5296–5310 (2014). https://doi.org/10.1039/C4SM00299G

[34] Finbloom, J.A., Demaree, B., Abate, A.R., Desai, T.A.: Networks of high aspect ratio particles to direct colloidal assembly dynamics and cellular interactions. Advanced Functional Materials **30**(48), 2005938 (2020) https://onlinelibrary.wiley.com/doi/pdf/10.1002/adfm.202005938. https://doi.org/10.1002/adfm.202005938

[35] Hueckel, T., Hocky, G., Sacanna, S.: Total synthesis of colloidal matter. Nature Reviews Materials **6**, 1–17 (2021). https://doi.org/10.1038/s41578-021-00323-x

[36] Wensink, R., Vroege, G.J.: Isotropic-nematic phase behavior of length polydisperse hard rods. The Journal of Chemical Physics **119** (2003). https://doi.org/10.1063/1.1599277

[37] Adams, D., Stutzmann, S., Stoudmann, C., Blokesch, M.: Dna-uptake pili of vibrio cholerae are required for chitin colonization and capable of kin recognition via sequence-specific self-interaction. Nature Microbiology **4**, 1–13 (2019). https://doi.org/10.1038/s41564-019-0479-5

[38] Secor, P.R., Michaels, L.A., Ratjen, A., Jennings, L.K., Singh, P.K.: Entropically driven aggregation of bacteria by host polymers promotes antibiotic tolerance in ¡i¿pseudomonas aeruginosa¡/i¿. Proceedings of the National Academy of Sciences **115**(42), 10780–10785 (2018) https://www.pnas.org/doi/pdf/10.1073/pnas.1806005115. https://doi.org/10.1073/pnas.1806005115

[39] Kunoh, T., Yamamoto, T., Prasad, M., Ono, E., Li, X., Sugimoto, S., Iida, E., Obana, N., Takeda, M., Nomura, N., Utada, A.S.: Porous pellicle formation of a filamentous bacterium, ¡i¿leptothrix¡/i¿. Applied and Environmental Microbiology **0**(0), 01341–22 https://journals.asm.org/doi/pdf/10.1128/aem.01341-22. https://doi.org/10.1128/aem.01341-22

[40] Tsurusawa, H., Leocmach, M., Russo, J., Tanaka, H.: Direct link between mechanical stability in gels and percolation of isostatic particles. Science Advances **5**(5), 6090 (2019) https://www.science.org/doi/pdf/10.1126/sciadv.aav6090. https://doi.org/10.1126/sciadv.aav6090

[41] Burel, C., Dreyfus, R., Gage, L.: Physical mechanisms driving the reversible aggregation of staphylococcus aureus and response to antimicrobials. Scientific Reports **11** (2021). https://doi.org/10.1038/s41598-021-94457-1

[42] Nigmatullin, R., Johns, M.A., Muñoz-García, J.C., Gabrielli, V., Schmitt, J., Angulo, J., Khimyak, Y.Z., Scott, J.L., Edler, K.J., Eichhorn, S.J.: Hydrophobization of cellulose nanocrystals for aqueous colloidal suspensions and gels. Biomacromolecules **21**(5), 1812–1823 (2020) https://doi.org/10.1021/acs.biomac.9b01721. https://doi.org/10.1021/acs.biomac.9b01721. PMID: 31984728

[43] Huang, J., Liu, S., Zhang, C., Xinyu, W., Pu, F., Ba, F., Xue, S., Ye, H., Zhao, T., Ke, L., Wang, Y., Zhang, J., Fan, C., Lu, T., Zhong, C.: Programmable and printable bacillus subtilis biofilms as engineered living materials. Nature Chemical Biology **15** (2019). https://doi.org/10.1038/s41589-018-0169-2

[44] Schaffner, M., Rühs, P.A., Coulter, F., Kilcher, S., Studart, A.R.: 3d printing of bacteria into functional complex materials. Science Advances **3**(12), 6804 (2017) https://www.science.org/doi/pdf/10.1126/sciadv.aao6804. https://doi.org/10.1126/sciadv.aao6804

[45] Yang, Y., Wang, Z., Gan, C., Klausen, L.H., Bonné, R., Kong, G., Luo, D., Meert, M., Zhu, C., Sun, G., Guo, J., Ma, Y., Bjerg, J., Manca, J., Xu, M., Nielsen, L.P., Dong, M.: Long-distance electron transfer in a filamentous gram-positive bacterium. Nature Communications **12**, 1709 (2021). https://doi.org/10.1038/s41467-021-21709-z

[46] Zoueki, C.W., Tufenkji, N., Ghoshal, S.: A modified microbial adhesion to hydrocarbons assay to account for the presence of hydrocarbon droplets. Journal of Colloid and Interface Science **344**(2), 492–496 (2010). https://doi.org/10.1016/j.jcis.2009.12.043

[47] Calabrese, V., Haward, S.J., Shen, A.Q.: Effects of shearing and extensional flows on the alignment of colloidal rods. Macromolecules **54**(9), 4176–4185 (2021) https://doi.org/10.1021/acs.macromol.0c02155. https://doi.org/10.1021/acs.macromol.0c02155

[48] Thompson, A.P., Aktulga, H.M., Berger, R., Bolintineanu, D.S., Brown, W.M., Crozier, P.S., in 't Veld, P.J., Kohlmeyer, A., Moore, S.G., Nguyen, T.D., Shan, R., Stevens, M.J., Tranchida, J., Trott, C., Plimpton, S.J.: LAMMPS - a flexible simulation tool for particle-based materials modeling at the atomic, meso, and continuum scales. Comp. Phys. Comm. **271**, 108171 (2022). https://doi.org/10.1016/j.cpc.2021.108171

[49] Hagberg, A., Swart, P., S Chult, D.: Exploring network structure, dynamics, and function using networkx. Technical report, Los Alamos National Lab.(LANL), Los Alamos, NM (United States) (2008)